Optimization of Spring Constant of a Pneumatic Artificial Muscle-Spring Driven Antagonistic Structure

Zhongchao Zhou, Shota Kokubu, Yuanyuan Wang, Yuxi Lu, Pablo Enrique Tortós, and Wenwei Yu

***Abstract*—Pneumatic artificial muscles (PAMs) have been widely applied to robotic systems, especially assistive devices, which could benefit from PAMs' intrinsic viscoelasticity. However, nonlinearity and hysteresis make it challenging to achieve high-accuracy control. Using pre-tensioned springs to replace one side PAMs in an antagonistic structure is one efficient way to improve control accuracy. However, in the previous study, the selection method for spring, especially the range of spring constant has not been sufficiently investigated. This study designed a method to find the optimal spring constant based on gradient descent algorithm; and verified it with prototype and simulation experiments. Results showed that the group with optimal spring constant leads to a faster response time, smaller overshoot, and lower steady-state error, which indicated that the proposed method could find optimal spring constant. Moreover, the sensitivity of PAMs dynamic model parameters to the optimal spring stiffness was investigated. This study provides insights to practical use of soft actuators.**

***Index Terms*—Soft robot applications, pre-tensioned spring, optimal spring constant.**

I. Introduction

THE upper limb prostheses are the assistive devices that improve the activities of daily living (ADL) and quality of life (QOL) for amputees by replacing the missing or lost limb both in appearance and functionality [1]. Creating upper limb prostheses that are comfortable and conform to the user's anatomy is a significant challenge. Since shoulder amputees cannot manipulate their prosthetic arm because of their much shorter residual limbs, an appropriate output force and range of motion (ROM) are much more important for a trans-humeral prosthesis (shoulder prosthesis) than hand and trans-radial prostheses [2].

Manuscript received October 11, 2021; accepted March 4, 2022. Date of publication March 24, 2022; date of current version April 13, 2022. This work was supported in part by a Grant-in-Aid for Scientific Research under Grant KAKENHI 19K22949 from MEXT/JSPS. This letter was recommended for publication by Associate Editor J. Koh and Editor K. Cho upon evaluation of the reviewers' comments. *(Corresponding author: Wenwei Yu.)*

Zhongchao Zhou, Shota Kokubu, Yuanyuan Wang, Yuxi Lu, and Pablo Enrique Tortós are with the Graduate School of Science and Engineering, Chiba University, Chiba 2638522, Japan (e-mail: zhouzhongchao@outlook.com; s.kokubu@chiba-u.jp; dakiso2017@gmail.com; yuxi.lu@chiba-u.jp; pablotortos19@gmail.com).

Wenwei Yu is with the Graduate School of Science and Engineering, Chiba University, Chiba 2638522, Japan, and also with the Center for Frontier Medical Engineering, Chiba University, Chiba 2638522, Japan (e-mail: yuwill@faculty.chiba-u.jp).

Digital Object Identifier 10.1109/LRA.2022.3162021

Shoulder prostheses are usually actuated by electric motors, which have drawbacks in terms of their weight, power consumption [1], [3], [4]. Moreover, the lack of compliance and safety also makes it difficult to use in clinical application [5]. Soft actuator-driven shoulder prostheses are rapidly gaining traction as a viable alternative due to their inherent safety, simplicity of design, and increased potential for portability and efficacy [6]–[8].

Pneumatic artificial muscles (PAMs), originated from Joseph L. McKibben [9], are a kind of soft compliant actuator that contracts when it is pressurized. PAMs have become one of the most suitable soft actuators for exoskeletons, robot arms, and shoulder prostheses, compared with other soft actuators [10]–[12], because they can achieve a sufficiently large force output to meet the requirements of shoulder prostheses when the air is pressurized [13] and PAMs have a higher power-to-weight ratio, a higher power-to-volume ratio [14], and a lower cost [15].

Inspired by the human muscle system, PAMs are often set up as antagonistic, allowing the adjustment of joints' stiffness and position [16]–[18]. The movement principle of an antagonistic structure is when one muscle contracts, the other relaxes. Unfortunately, motion control of PAMs remains a challenge due to their nonlinearity [19]–[21], especially, antagonistic arrangement requires the simultaneous control of two sides of PAMs, which causes several problems, i.e., difficulty to achieve accurate force and motion control, and slow responses to control inputs. Moreover, dual-PAMs antagonistic structure increases mechanical design and control complexity, and makes the device/system bulky, heavy, and even expensive, which is unsuitable for wearable devices [22].

One way to meet the requirements is to reduce the number of PAMs used in the antagonistic structure. In [23], authors proposed a method to find optimal spring constant in a motor-driven antagonistic structure. However, this method has not been proven to be useful for antagonistic joints driven by PAMs. In [24], mechanism which used single-PAM with a spring was designed. In the study, a sliding mode controller was designed based on a PAMs - torsion spring dynamic model. They also proposed a method to confirm the spring constant's appropriate range and confirmed its effectiveness by simulation results. However, the method is based on time-varying parameters, which implies that the range of the spring constant altered over time. The proposed method is inappropriate for practical use, and

they made no mention of the range's optimal spring constant. Moreover, the prototype experiment was not done to verify their hypothesis. In [25], PAMs-spring antagonism is applied to a robotic leg, it was mentioned that spring constants should be large enough to withstand perturbations when robotic leg is in a balance state. However, spring constant selection method was not addressed. T Tsai *et al.* used a novel mechanism consisting of one PAM combined with a torsion spring [20]. The experimental results showed that the innovative single-PAM with torsion springs mechanical arm system architecture can achieve the same effect as the dual-PAM-driven joint antagonistic structure. However, they only used one group of torsion spring, and did not give an analysis for spring constant. In [22], a novel wearable device driven by a new PAMs-Torsion Spring (TS) joint was proposed. However, more experiments need to be implemented to improve the accuracy and stability of the angle/position control, and the spring constant has not been investigated in their research. Generally, previous studies primarily have focused on PAMs in PAMs-spring antagonistic structures and their controller. The performance under different spring constants was not compared and analyzed. Three types of joint spring-PAMs structures were proposed in [26], and the results demonstrated that pre-tensioned springs could compensate for the PAMs' nonlinearity and improve response time and control accuracy, indicating the importance of pre-tensioned springs. Additionally, it was stated that the existence of an optimal spring constant that results in optimal system performance. However, the method to determine the optimal spring constant has not been proposed.

In this study, we verified that different spring constants in a PAMs-spring antagonistic structure would lead to different performances. A method to find optimal spring constant using a gradient descent algorithm was proposed. The optimal spring constant in the novel PAMs-spring antagonistic structure was calculated and was verified both in simulation and prototype experiments.

This paper is organized as follows. Section II introduces the novel PAMs-spring antagonistic structure calculation, including its dynamic model, sliding mode controller, and discretization for state-space function. Section III introduces the optimal method for spring constant based on the gradient descent algorithm. Section IV explains the simulation and prototype experiment setting. Section V and VI give the results and discussion. The last section produces the conclusion and future work.

II. Modelling

A. Dynamical Model of PAMs-Actuated Robots

According to [9], PAMs can be modeled as three elements connected in parallel: a spring, a damper, and a contractile element, as shown in Fig. 1.

The functions of the three elements are given by

$$K^*\ (P) = K_0\ + K_1 P, \tag{1}$$

$$B\ (P) = B_0\ + B_1 P\ \text{(Inflation)} \tag{2}$$

$$B\ (P) = B_2\ + B_3 P\ \text{(Deflation)}, \text{ and} \tag{3}$$

$$F\ (P) = F_0\ + F_1 P. \tag{4}$$

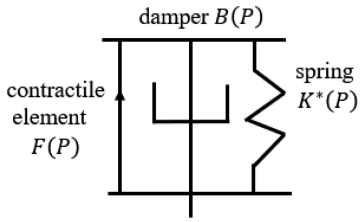

Fig. 1. A three-element model of the PAMs.

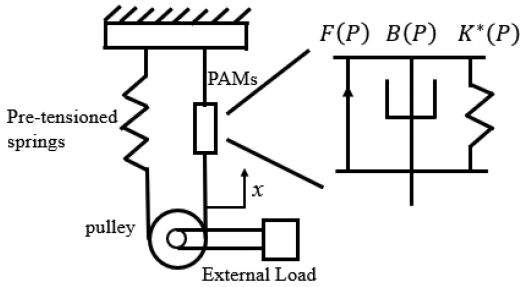

Fig. 2. Novel pre-tensioned PAMs-spring antagonistic structure.

The total force exerted by the muscles is

$$R\ =\ F\,(P) - B\,(P)\,\dot{x} - K^*\,(P)\,x \tag{5}$$

where $K_0\,, K_1,\ B_0\,, B_1,\ B_2\,, B_3,\ F_0\,, F_1$ need to be realized by experiment; *R* is the total force exerted; *P* is the internal pressure; *F* is the force exerted by the contractile element; $B(P)$ is the damping coefficient; and $K^*(P)$ is the spring coefficient; *x* is the displacement in relation to the global origin. *R* and *x* are functions of the time, *t*.

B. Dynamical Model of PAMs-spring Antagonistic Structure

The novel PAMs-spring antagonistic structure is shown in Fig. 2, in which left side is a spring, right side is a PAM.

Next, the dynamical model and state-space functions were considered. The dynamical model of Fig. 2 can be described as

$$(F\,(P) - K^*\,(P)\,x - B\,(P)\ \dot{x} - K_L\,x\,)\,r\ =\ J\alpha + MgL\sin\frac{x}{r} \tag{6}$$

where, $J\ =\ \frac{1}{2}\ mr^2$

Here, *J* is the moment of inertia; α is the angular acceleration; *M* is the external load; *L* is the rod length; *m* is the pulley mass; *r* is the pulley radius; K_L is spring constant of left pre-tensioned springs.

C. Sliding Mode Controller

The sliding mode controller for the novel PAMs-spring antagonistic structure was developed as follows. Substituting Equations (1)–(4) into Equation (6) and simplifying, the state-space function is obtained as follows:

$$\begin{aligned} \dot{x}_2 &= x_2 \\ \dot{x}_2 &= \frac{2[(F_0 - F_{\mathrm{L}}) - (K_0 + K_L)x_1 r - B_0 x_2 r + (F_1 - K_1 x_1 \mathrm{r} - B_1 x_2 r)u]}{mr} \\ &\quad - \frac{2MgLsinx_1}{mr^2} \end{aligned} \tag{7}$$

where x_1 is the rotation angle, x_2 is the derivative of x_1 , F_L is pre-tensioned force made by left side pre-tensioned spring. u is output of controller, which means air pressure. Throughout this paper, for the simplicity of expression, we make the following substitution:

$$f\ (x) = \frac{2(F_0 - F_{\mathrm{L}})}{mr} - \frac{2\left(K_0 + K_L\right)x_1}{m} - \frac{2B_0x_2}{m} - \frac{2MgLsinx_1}{mr^2} \tag{8}$$

$$g\ (x) = \frac{2\left(F_1 - K_1x_{1\mathrm{r}} - B_1x_2r\right)}{mr} \tag{9}$$

The state-space function is obtained as follows:

$$\dot{x}_1 = x_2 \tag{10}$$

$$\dot{x}_2 = f(x) + g(x)\,u \tag{11}$$

setting x_{1d} as the desired angle, and *e* as the error,

$$e = x_{1d} - x_1 \tag{12}$$

Δ represents the error between the desired and actual angular velocities:

$$\Delta = x_{2d} - x_2 \tag{13}$$

In this paper, x_{2d} is set to $x_2d = \dot{x}_{1d} + c_1e$

According to the law of sliding mode control, the output can be expressed as

$$u = \frac{1}{g(x)}\left(e + \ddot{x}_{1d} + C_1\dot{e} - f(x) + C_2sgn(x) + C_3\Delta\right) \tag{14}$$

where C_1, C_2, C_3 is control gain, $sgn(x)$ is sign function. In order to ensure the stability of the system, control gain needs to satisfy $C_1, C_2, C_3 > 0$.

D. Discretization for State-Space Function

Since the simulation environment is performed in a discrete state, discretize state-space function was proposed. Matrix form state space function is shown as follow:

$$\begin{pmatrix}\dot{x}_1\\ \dot{x}_2\end{pmatrix} = \begin{pmatrix}0 & 1\\ \frac{-2(K_0+K_L)}{m} & -\frac{2B_0}{m}\end{pmatrix}\begin{pmatrix}x_1\\ x_2\end{pmatrix} + \begin{pmatrix}0\\ \frac{2(F_1-K_1x_{1\mathrm{r}}-B_1x_2r)}{mr}\end{pmatrix}u + \begin{pmatrix}0\\ \frac{2(F_0-F_{\mathrm{L}})}{mr} - \frac{2MgLsinx_1}{mr^2}\end{pmatrix}$$

Throughout this paper, for the simplicity of expression, we make the following substitution:

$$\dot{x} = Ax + Bu + C \tag{15}$$

According to the Forward Euler Method [26], Equation (15) can be changed into

$$\dot{x}\ (i) = A(i)x(i) + B(i)\,u(i) + c(i) \tag{16}$$

where i is the number of iterations, according to the definition of a derivative, Equation (16) can be described as follows:

$$\dot{x}\ (i) = \frac{x(i+1) - x\ (i)}{T} \tag{17}$$

where *T* is time step, substituting Equation (16) into (17) yields Equation (18)

$$\dot{x}\ (i) = A(i)x(i) + B(i)\,u(i) + c\ (i) = \frac{x(i+1) - x\ (i)}{T} \tag{18}$$

For further simplification, the discretization of state-space function can be described as Equation (19)

$$x\ (i+1) = (I + AT)\,x(i) + BTu(i) + TC(i) \tag{19}$$

where *I* is identity matrix.

III. Method for Acquiring Optimal Spring Constant

A. Cost Function

In order to find the optimal spring constant *K*, the error function is set as follow:

$$e(i,K)\ = \begin{cases} xd(i,K) - x(i,K),\ xd > x \\ \alpha\left(x(i,K) - xd(i,K)\right),\ x > xd \end{cases} \tag{20}$$

where α is the discount factor.

α reflects the proportion of overshoot and response speed. The larger α means that the error function is more sensitive to overshoot and less sensitive to response time. In this research, α would be set as 2.

Summing up the error function (20) according to the number of time iterations gives the cost function $f(K)$ showed in function (21):

$$f\ (K) = \begin{cases} \sum_{i=0}^{S} e(i,K), K > 0 \\ 10e10 + |K|,\ K \le 0 \end{cases} \tag{21}$$

where *S* is total number of iterations, in this paper, *S* was set to 4. Since the gradient descent can only get an unconstrained optimal solution. In this paper, a big cost function value was set when $K \le 0$ to ensure optimal spring constant K is meaningful.

Approximating derivatives of Equation (21) was calculated by Finite Difference Method (FDM) [27], which can be described as Equation (22)

$$\frac{\partial f(K)}{\partial K_0} \approx \frac{f\left(K + \frac{\Delta K_0}{2}\right) - f\left(K - \frac{\Delta K_0}{2}\right)}{\Delta K_0} \tag{22}$$

where K_0 is the place to be derived and ΔK_0 is the spring constant increment, the value of ΔK_0 close to zero.

B. Gradient Descent for Optimal Spring Constant

Gradient descent is one of the most popular algorithms to perform optimization [28]. According to Yang *et al.* [29], the Gradient descent with Momentum (GDM) has a faster convergence speed than traditional Gradient descent (GD), the process can be summarized as

---

Initialize $vdb = 0$
Do
$vdb = \beta vdb + (1 - \beta)\frac{\partial f(K)}{\partial K_0}$
$K(i+1) := K(i) - \varepsilon^* vdb$
until $K(i+1) - K(i) \le \delta$

TABLE I
DIFFERENT FIXED CONSTANT WITH DIFFERENT LOCATION OF *K*

	K>5000	200 < *K* ≤ 5000	50 < *K* ≤ 200	10 < *K* ≤ 50	0 < *K* ≤ 10
v_1	1000	200	100	60	30
v_2	100	50	30	1	1

where β is the momentum term, δ is minimum iteration error δ, ε is step size.

GDM often inevitably falls into local optimal solutions. This was dealt with by adopting the random walk method, and beginning with different spring constant *K* [30] regarding the local optimal solution.

In the real application, the range of spring constant is from 0 -10000 *N/m*. In this study, the optimal spring constant *K* was calculated in the range of 0 -10000 *N/m*.

For the different spring constant, five initial spring constants were selected, as shown in Section V.

For random walk, two problems that must be solved are determining when the optimization is stuck in a local optimum and defining the random walk. A heuristic is used to recognize a local optimal *K*, $|K(i) - K(i+1)| < \epsilon$ assuming that $K(i)$ is near a local optimal *K*. Randomized potential planner (RPP) was used to define the random walk, in which each random walk consists of 2 random steps. A random step from $K = (K_1,\ K_2)$ is obtained by randomly adding fixed constants to each *K*,

$$K_{random-step} = (K \pm v_1, K \pm v_2)$$

where *v1,v2* are fixed constants, and were selected by trial and error based on the location of *K*, the constants are shown in Table I.

IV. SIMULATION EXPERIMENT SETTLING SYSTEM DESCRIPTION

A. Simulation Experiment Setting

First, the parameters for verifying the effectiveness of the proposed structures and controller were determined, as shown in Table II.

All the values of the PAMs' coefficients were obtained through measurements of the pneumatic actuator PM-10P (SQUSE), which weights 3g for each, can provide a high output force (maximum tension of 100 N), and has an average shrinkage ratio of 30% per piece (around 2 cm for each). The negative sign of B_2 and B_3 indicates movement in the direction opposite to the positive. The pulley used in this study was Model P36MXL6.4B pulley (Mitsuboshi Belting Ltd., Japan), of which mass is about 5g and radius *R* is 5mm. With the results of an identification experiment, the time step *T* of the simulation was set to 0.035s. All the models were implemented using MATLAB (MathWorks, R2019b).

B. Prototype Experiment Setting

The controllers were designed based upon several structures and then verified. Novel PAMs-spring antagonistic structure was used to verify the designed SMC controller with different spring constant *K*.

TABLE II
COEFFICIENT SETS USED FOR THE SIMULATION

No.	constant	value	unit
1	F_0	15	N
2	F_1	200	N
3	K_0	40	N/m
4	K_1	2	N/m
5	B_0	20	Ns/m
6	B_1	9	Ns/m
7	B_2	-8	Ns/m
8	B_3	-3	Ns/m
9	m	15	g
10	R	5	mm
11	K_L	200	N/m
12	M	0	Kg
13	F_L	15	N
14	L	1	cm

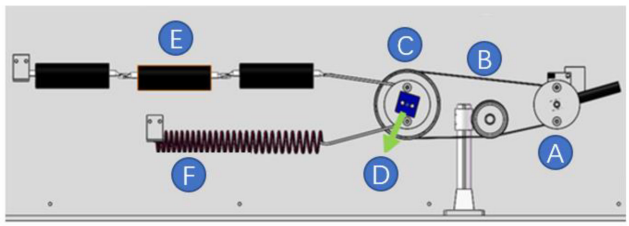

Fig. 3. 3D model of PAMs-spring antagonistic structure.

Fig. 3 showed the 3D model of novel PAMs-spring antagonistic structure driven by the PAMs (Part E) arranged in serial. The PAMs and pre-tensioned spring (Part F) formed the antagonistic structure. The PAMs drove the driving pulley (Part C) during inflation, and its angle of rotation and angular velocity were then transmitted to the controller through an MPU6050 six-axis sensor (Part D, TDK InvenSense Corp., San Jose, CA, USA) by an inter-integrated circuit (IIC) bus. The sampling time of the sensor was set to 0.035s, same as the time step *T* in simulation setting. Part B served as the tensioning wheel, and the belt rotated the driven pulley (Part A).

The data of angle and angular velocity were sent to the computer via the serial port. PAMs have a limited range of motion (RoM), so three PAMs were arranged in serial and the timing belt structure was developed to increase the RoM of PAMs-spring antagonistic structure, which was determined from 0 rad to 4.012 rad (230°).

TABLE III
DIFFERENT INITIAL SPRING CONSTANT

K_i	10	100	2000	5000	10000
Optimal K	318 N/m	317 N/m	320 N/m	321 N/m	319 N/m
Cost function	11.08 rad	11.08 rad	11.08 rad	11.08 rad	11.08 rad

C. Control Process Design

The main control chip was an STM32 integrated circuit (STMicroelectronics, Geneva, Switzerland). The air proportional valve used is SMC ITV0030-2ML (SMC Pneumatics Ltd., U.K.), we noticed that, even if the maximum input pressure of the proportional valve was set to the same value for desired angle (e.g., 200 *kPa* for 50 degree) by an air regulator (Manufacturer model number: AW20-01BE-B, SMC), the input pressure of the proportional valve would significantly first decrease then gradually recover, which will influence the response speed. After trial and error, the maximum pressure of the proportional valve was set to 230 *kPa* by the air regulator to ensure that the maximum pressure did not fall below 200 *kPa*.

The PAMs were PM-10P (SQUSE). The difference between the actual and desired angle was input to the designed SMC controller to obtain the necessary air pressure.

Although the air pressure proportional valve was nonlinear, its nonlinearity was not extensively considered in this study. Instead, a compensation method was adopted to calibrate the air pressure to provide the required pulse-width-modulation (PWM) value. The polynomial trendline function as follow:

$$Y = -0.0001P^3 + 0.0477P^2 - 6.5417P + 788.89$$

where P is the air pressure; Y is the PWM value; $R^2 = 0.9902$.

V. RESULTS

A. Simulation Results

The initial state was set as $x_1 = 0, x_2 = 0$, in all simulations, the output range was 0 – 200 *kPa*. Desired angle $x_d = 0.877$ rad (around 50°). Different spring constants in the range of 0-10000 (*N/m*, The unit of spring constant is *N/m*, which will be omitted in the following text), were taken into simulation model. The optimal spring constant was calculated by proposed method with the $\beta = 0.9$, $\delta =$ 10e-5, $\varepsilon = 1$. Moreover, five different initials K_i was set as in Table III to avoid GDM falls into the local optimal solution. The convergence graph was shown in Fig. 4, with the initial spring constant 10000.

Table III showed that the optimal spring constant K was converged at $K = 320$ with the total cost function 11.08 rad. The process converged within 350 iterations. The performance of 4 spring constants, 60, 600, 2000, 8000 was compared with that of the optimal spring constant, 320.

The simulation results in Fig. 5. and Table IV showed that the group with optimal spring constant can achieve the faster response time as well as the smallest total error, which reflects that through the proposed method, the optimal spring constant can be acquired.

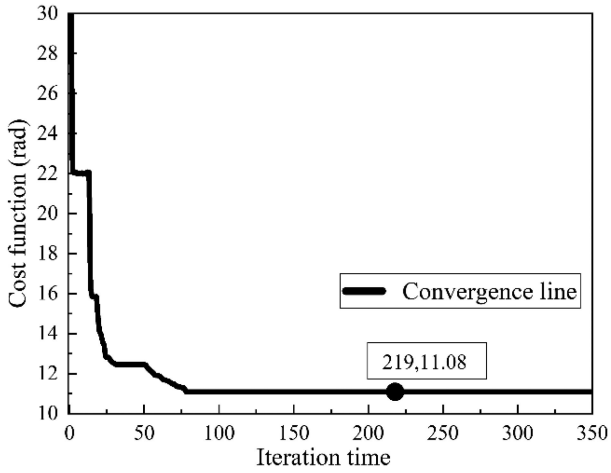

Fig. 4. Convergence graph with the initial spring constant is 10000.

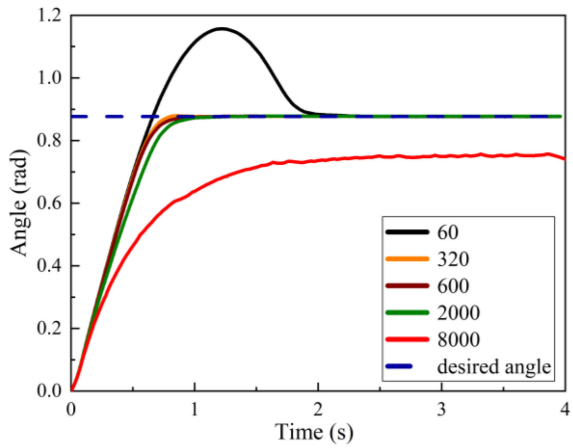

Fig. 5. Simulation performance of different spring constant.

B. Prototype Experiment

Since it is difficult to obtain springs with exact spring constant $K = 320$ in the real application, spring with $K = 300$ was used to replace $K = 320$ as the optimal spring. We have verified that there is little difference between $K = 320$ and 300 in simulations. Prototype results can be seen from Fig. 6. The performance of simulation and prototype was shown in Table IV.

The results showed that when $K = 300$, which is the nearest for the optimal spring constant calculated by the proposed method. The performance is the best with the fastest response time, nearly no steady-state error and overshoot.

Because $K = 600$ is close to the optimal spring constant, the rising and settling times, overshoot, as well as the steady-state error, are likewise acceptable.

For the prototype performance when $K = 60$, which means the spring constant was too small, although delay time is faster than when K = 300 or 600, bigger overshoot occurred, which is unacceptable in real application.

TABLE IV
RESPONSE UNDER OPTIMAL SPRING CONSTANT COMPARE WITH OTHERS:SIMULATION (PROTOTYPE)

Spring constant (N/m)	60	300	600	2000	8000
Overshoot (rad)	0.28 (0.17)	0.002 (0.01)	0 (0.008)	0 (0)	0 (0)
Settling time (ms)	1560 (1352)	770 (930)	805 (1050)	840 (1385)	∞ (∞)
Delay time (ms)	385 (528)	400 (560)	420 (680)	508 (732)	533 (870)
Steady-state error (rad)	0 (0.02)	0 (0.02)	0 (0.03)	0 (0.02)	0.12 (0.27)

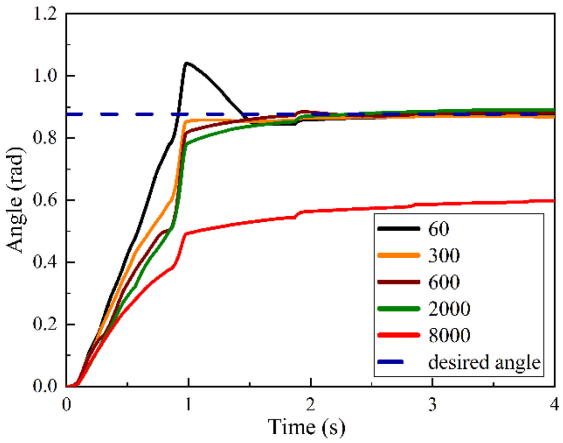

Fig. 6. Prototype performance of different spring constant.

TABLE V
TOTAL ERROR BETWEEN SIMUTION AND PROTOTYPE

Spring constant K (N/m)	Simulation (rad)	Prototype (rad)
$K = 60$	22.573	19.321
$K = 300$	11.084	16.566
$K = 600$	11.241	17.818
$K = 2000$	11.637	19.247
$K = 8000$	28.027	48.890

When $K = 2000$, the spring constant is significantly larger than the optimal spring constant, resulting in a slower response time. Slow response times will make real-time operation of shoulder prostheses difficult. The total error between simulation and prototype were compared in Table V.

According to Table V, when spring constant is the optimal one, the minimal total error could be obtained in both simulation and prototype experiments. However, there are still some differences between the total error of the simulation and that of the prototype.

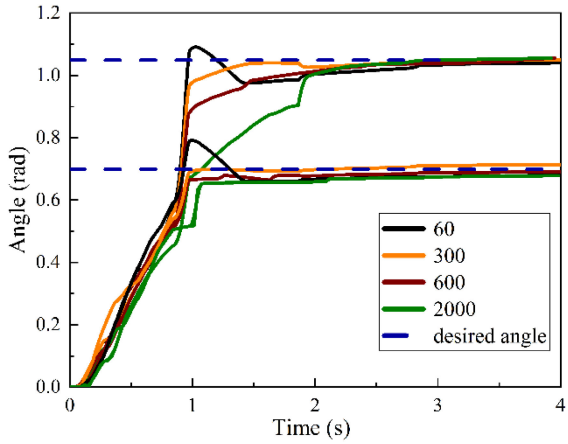

Fig. 7. Prototype experiment under 0.698 rad and 1.047 rad.

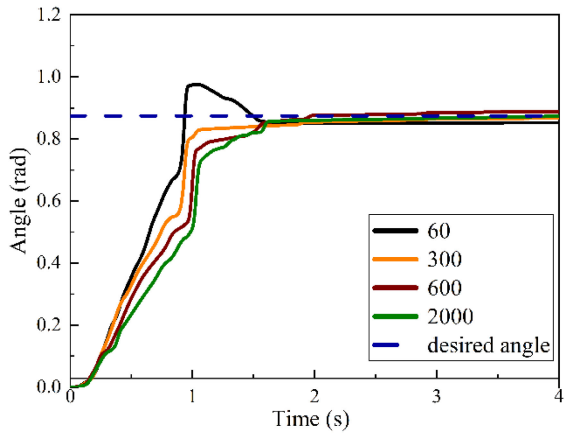

Fig. 8. Prototype experiment's step response to external load.

The tendency of all step-response characteristic is the same, which agrees with what was shown in Fig. 5: when the K is smaller than the optimal value, the performance changes drastically, while K is larger than the optimal value, the performance changes gradually. This indicate that our proposed simulation method is reliable.

C. Additional Experiments to Verify Optimal Spring Constant

To determine whether the optimal spring constant takes effect on different desired angles, the following prototype experiments were conducted: the desired angles were set to 0.698 rad and 1.047 rad (about 40° and 60°), respectively. The other parameters remained the same as those of the previous. Since it was made clear that when the spring constant $K = 8000$, the system is incapable of tracking the desired angle, thus this was not included in this part. The results were shown in Fig. 7.

In order to investigate the effect of the optimal spring constant under different load, and the possibility of force control at a certain desired angle, an external load 250 g was added to system and step responses were measured for different spring constants. the desired angle was set to 0.877 rad (50°). The results were shown in Fig. 8.

TABLE VI
VALUE FOR EACH PARAMETER

m	1	2	3	4
ΔB_0^m	20	10	-10	-20
ΔK_m	74	40	-80	-20

TABLE VII
SENSITIVITY OF DYNAMIC MODEL TO OPTIMAL SPRING CONSTANT

Parameter	Sensitivity	Parameter	Sensitivity
K_0	1.000	B_1	17.062
K_1	5.612	F_0	0.686
B_0	4.175	F_1	1.088

According to the Fig. 7 and 8, additional experiments demonstrated that regardless of the angle, load, $K = 300$ can still be the optimal spring constant. The group with $K = 2000$ becomes very slow when the desired angle is 1.047 rad because the pressure is nearly at the maximum air pressure.

D. Sensitivity Between Dynamical Model and Optimal Spring Constant

In order to figure out the relationship between PAMs' dynamical mode and optimal spring constant. The sensitivity of B_0 to the optimal spring constant *K*, as an example, is shown as follow:

$$S = \frac{\sum_{m=1}^{n} \left| \frac{\Delta K_1}{\Delta B_0^1} \right| + \left| \frac{\Delta K_2}{\Delta B_0^2} \right| + \left| \frac{\Delta K_3}{\Delta B_0^3} \right| + \cdots + \left| \frac{\Delta K_m}{\Delta B_0^m} \right|}{n} \tag{23}$$

where ΔB_0^m is the variation refer to standard B_0 shown in Table II. ΔK_m is the variation for optimal spring constant corresponds to ΔB_0^m. *n* is the number variation for B_0. The value for each parameter is shown in Table VI.

In this paper, sensitivity between the optimal spring constant and PAMs' dynamical model K_0, K_1, B_0 , B_1, F_0 , F_1 were investigated. The range of all the parameters variation of the dynamical model was identical to B_0, the formula is the same as Equation (23). The results are shown in Table VII.

According to Table VII, parameter B_1 has the greatest sensitivity (17.062) to the optimal spring constant, which implies that when B_1 is changed by 1 Ns/m, the optimal spring constant changes by 17.062 N/m, indicating that adjusting B_1 has the biggest effect on the optimal spring constant.

VI. DISCUSSION

A better selection for spring constant in a novel PAMs-spring antagonistic structure would lead to better performance. Fig. 5 and 6 demonstrated that a smaller *K* results in a greater maximum overshoot due to the increased damping ratio. In comparison, if *K* is set too high, the system is unable to follow the desired angle, indicating that a high spring constant increases steady-state inaccuracy.

We proposed a discrete state-space function for a novel PAMs-spring antagonistic structure and its SMC controller. Moreover, a cost function of error and spring constant was proposed. According to the proposed cost function, optimal spring constant can be calculated based on the gradient descent.

Five initial spring constants shown in Table III were selected to find the optimal spring constant. The results showed that the optimal spring constant was converged at around $K = 320$.

Table IV showed that the system with optimal spring constant would lead to a faster response time and smaller steady-state error although the overshoot is not the smallest. In the cost function, the discount factor α was set as 2, which is not big enough to eliminate overshoot. In the future, discount factors need to be considered based on human actions.

Figs. 5, 6 and Tables IV, V showed that the optimal spring constant is suitable for simulation and prototype. The performance of prototype experiment is worse than that of the simulation. Especially the response time of the prototype is slower than that of the simulation (by approximately 200 –500 ms, depending on the value of *K*) and the value of total error of prototype is bigger than that in simulation. That can might be attributed to the nonlinearity of the proportional valve and friction, etc. In this paper, the multiple pairs of input PWM to proportional valve and output air pressure air pressure were recorded and used as a lookup table to calculate the necessary input PWM to proportional valve by interpolation. This didn't take into consideration the nonlinearity such as delay and dead zone. The settling time at $K = 2000$ is not significantly different from its at $K = 320$ in the simulation, but the difference becomes quite large in the prototype, despite the fact that the tendencies are identical, indicating that prototype performance is more sensitive to the optimal spring constant than simulation performance. As a result, it is more critical to determine the optimal spring constant for the real application.

The results of the additional experiments shown in Figs. 7, 8 demonstrated that the optimal spring constant resulted in the best performance in a variety of situations, which implied that, the optimal spring constant depends on the characteristic (such as damping ratio and natural frequency) of the system itself.

The sensitivities (Table VII) of F_0, F_1, K_0 are almost 1, indicate that optimal spring constant varies almost in the same way as these three parameters. K_1 and B_0 have sensitivities of roughly 5, which means that when K_1 and B_0 change, the optimal spring constant changes by a factor of five. B_1 has the maximum sensitivity to changes in optimal spring constants, indicating that adjusting B_1 has the biggest effect on the optimal spring constant, if external damage or manufacturing procedures cause $B_1$to vary greatly, the opitmal spring constant *K* also changes significantly, forcing recalculation. In practice, it is crucial to maintain the stability of the B_1 term.

VII. CONCLUSION AND FUTURE WORK

In this paper, we proposed a method to find the optimal spring constant of a novel PAMs-spring antagonistic structure. Through the method, the optimal spring constant was calculated and evaluated by simulation and prototype experiments. The experiment results showed that the optimal spring constant led to better performance: faster response time and smaller error. Moreover, sensitivity between PAMs' dynamic model and optimal spring constant indicated that one parameter influences optimal spring

constant significantly, which needs to be designed stably in real application.

In the future, the PAMs-spring antagonistic structure with multiple degrees of freedom shall be studied.

REFERENCES

[1] Y. Furuya, T. Mikami, T. Suzuki, and Y. Fujimoto, "On an active prosthetic knee joint driven by a high thrust force helical motor," in *Proc. IIECON-39th Annu. Conf. IEEE Ind. Electron. Soc.*, 2013, pp. 5894–5899.

[2] M. Sekine, K. Shiota, K. Kita, A. Namiki, and W. Yu, "A lightweight shoulder prosthesis with antagonistic impact-absorbing hybrid actuation for bimanual activities of daily living," *Adv. Mech. Eng.*, vol. 8, no. 4, pp. 1–17, Mar. 2016.

[3] P. J. Kyberd *et al.*, "Two-degree-of-freedom powered prosthetic wrist," *J. Rehabil. Res. Dev.*, vol. 48, no. 6, pp. 609–618, Aug. 2011.

[4] M. D. Twardowski, S. H. Roy, Z. Li, P. Contessa, G. De Luca, and J. C. Kline, "Motor unit drive: A neural interface for real-time upper limb prosthetic control," *HHS Public Access*, vol. 16, no. 1, pp. 1–28, Feb. 2020.

[5] H. Xie, Z. Li, and F. Li, "Bionics design of artificial leg and experimental modeling research of pneumatic artificial muscles," *J. Robot.*, vol. 2020, Nov. 2020, Art. no. 3481056.

[6] C. Y. Chu and R. M. Patterson, "Soft robotic devices for hand rehabilitation and assistance: A narrative review," *J. Neuroeng. Rehabil.*, vol. 15, no. 1, pp. 1–14, Feb. 2018.

[7] A. Capace, C. Cosentino, F. Amato, and A. Merola, "A multistate friction model for the compensation of the asymmetric hysteresis in the mechanical response of pneumatic artificial muscles," *Actuators*, vol. 8, no. 2, pp. 49–59, Jun. 2019.

[8] S. Allen, "New prostheses and orthoses step up their game: Motorized knees, robotic hands, and exosuits mark advances in rehabilitation technology," *IEEE Pulse*, vol. 7, no. 3, pp. 6–11, May 2016.

[9] D. B. Reynolds, D. W. Repperger, C. A. Phillips, and G. Bandry, "Modeling the dynamic characteristics of pneumatic muscle," *Ann. Biomed. Eng.*, vol. 31, no. 3, pp. 310–317, Jan. 2003.

[10] S. Ikemoto, Y. Kimoto, and K. Hosoda, "Shoulder complex linkage mechanism for humanlike musculoskeletal robot arms," *Bioinspiration Biomimetics*, vol. 10, no. 6, Oct. 2015, Art. no. 066009.

[11] L. Zhong, Z. Song, N. Sun, and Y. Qin, "Design and modeling of bionic robot arm actuated by pneumatic artificial muscles," in *Proc. 9th IEEE Int. Conf. Cyber Technol. Autom. Control Intell. Syst. CYBER*, 2019, pp. 389–394.

[12] X. Zang, Y. Liu, S. Heng, Z. Lin, and J. Zhao, "Position control of a single pneumatic artificial muscle with hysteresis compensation based on modified Prandtl-Ishlinskii model," *Biomed. Mater. Eng.*, vol. 28, no. 2, pp. 131–140, Mar. 2017.

[13] C. Majidi, "Soft robotics: A perspective - Current Trends and prospects for the future," *Soft Robot.*, vol. 1, no. 1, pp. 5–11, Jul. 2014.

[14] C. P. Chou and B. Hannaford, "Static and dynamic characteristics of McKibben pneumatic artificial muscles," in *Proc. IEEE Int. Conf. Robot. Automat.*, 1994, vol. 1, pp. 281–286.

[15] S. Hussain, S. Q. Xie, and P. K. Jamwal, "Adaptive impedance control of a robotic orthosis for gait rehabilitation," *IEEE Trans. Cybern.*, vol. 43, no. 3, pp. 1025–1034, Jun. 2013.

[16] T. Karnjanaparichat and R. Pongvuthithum, "Adaptive tracking control of multi-link robots actuated by pneumatic muscles with additive disturbances," *Robotica*, vol. 35, no. 11, pp. 2139–2156, Oct. 2017.

[17] X. Zhao, H. Ma, D. Ye, and D. Zhang, "Independent stiffness and force control of antagonistic pneumatic artificial muscles joint," in *Proc. 2nd Int. Conf. Adv. Robot. Mechatronics, ICARM*, 2017, pp. 734–739.

[18] G. Andrikopoulos, G. Nikolakopoulos, and S. Manesis, "Advanced nonlinear PID-based antagonistic control for pneumatic muscle actuators," *IEEE Trans. Ind. Electron.*, vol. 61, no. 12, pp. 6926–6937, Apr. 2014.

[19] F. Daerden and D. Lefeber, "Pneumatic artificial muscles: Actuators for robotics and automation," *Eur. J. Mech. Environ. Eng.*, vol. 47, no. 1, pp. 10–21, 2002.

[20] T. C. Tsai and M. H. Chiang, "Design and control of a 1-DOF robotic lower-limb system driven by novel single pneumatic artificial muscle," *Appl. Sci.*, vol. 10, no. 1, pp. 43–64, Dec. 2020.

[21] H. P. H. Anh, C. Van Kien, N. N. Son, and N. T. Nam, "New approach of sliding mode control for nonlinear uncertain pneumatic artificial muscle manipulator enhanced with adaptive fuzzy estimator," *Int. J. Adv. Robotic Syst.*, vol. 15, no. 3, pp. 1–11, Mar. 2018.

[22] J. Wu, J. Huang, Y. Wang, and K. Xing, "A wearable rehabilitation robotic hand driven by PM-TS actuators," *Intell. Robot. Appl.*, vol. 6425, pp. 440–450, Nov. 2010.

[23] Y. F. Lee, C. Y. Chu, J. Y. Xu, and C. C. Lan, "A humanoid robotic wrist with two-dimensional series elastic actuation for accurate force/torque interaction," *IEEE/ASME Trans. Mechatronics*, vol. 21, no. 3, pp. 1315–1325, Jun. 2016.

[24] K. Xing, J. Huang, J. He, Y. Wang, Q. Xu, and J. Wu, "Sliding mode tracking for actuators comprising pneumatic muscle and torsion spring," *Trans. Inst. Meas. Control*, vol. 34, no. 2/3, pp. 255–277, Jul. 2012.

[25] I. F. Lee *et al.*, "Squat and standing motion of a single robotic leg using pneumatic artificial muscles," *J. Appl. Sci. Eng.*, vol. 18, no. 4, pp. 363–370, Dec. 2015.

[26] Z. Zhou, Y. Wang, and W. Yu, "The role of pre-tensioned springs in 3 pneumatic artificial muscles driven joint mechanisms with sliding mode controllers," *Rob. Auton. Syst.*, vol. 151, Jan. 2022, Art. no. 104017.

[27] B. N. Biswas, S. Chatterjee, S. P. Mukherjee, and S. Pal, "A discussion on euler method: A review," *Electron. J. Math. Anal. Appl.*, vol. 1, no. 2, pp. 294–317, Jun. 2013.

[28] S. Ruder, "An overview of gradient descent optimization algorithms," 2016, *arXiv:1609.04747*.

[29] T. Yang, Q. Lin, and Z. Li, "Unified convergence analysis of stochastic momentum methods for convex and Non-convex optimization," 2016, *arXiv:1604.03257*.

[30] M. W. Spong, S. Hutchinson, and M. Vidyasagar, *Robot Modeling and Control*. New York, NY, USA: Wiley, 2006, ch. 5, pp. 93–100.